



# Acceleration of Cooling of Ice Giants by Condensation in Early Atmospheres

Kenji Kurosaki<sup>1,2</sup> and Masahiro Ikoma<sup>1,3</sup>

<sup>1</sup> Department of Earth and Planetary Science, Graduate School of Science, The University of Tokyo, 7-3-1 Hongo, Bunkyo-ku, Tokyo 113-0033, Japan; [kurosaki.k@nagoya-u.jp](mailto:kurosaki.k@nagoya-u.jp), [ikoma@eps.s.u-tokyo.ac.jp](mailto:ikoma@eps.s.u-tokyo.ac.jp)

<sup>2</sup> Department of Physics, Nagoya University, Furo-cho, Chikusa-ku, Nagoya-shi, Aichi 464-8602, Japan

<sup>3</sup> Research Center for the Early Universe, Graduate School of Science, The University of Tokyo, 7-3-1 Hongo, Bunkyo-ku, Tokyo 113-0033, Japan

Received 2017 January 31; revised 2017 March 24; accepted 2017 April 24; published 2017 May 22

## Abstract

The present infrared brightness of a planet originates partly from the accretion energy that the planet gained during its formation and hence provides important constraints to the planet formation process. A planet cools down from a hot initial state to the present state by losing energy through radiative emission from its atmosphere. Thus, the atmospheric properties affect the planetary cooling rate. Previous theories of giant planet cooling assume that the atmospheric composition is unchanged throughout the evolution. Planet formation theories, however, suggest that the atmospheres especially of ice giants are rich in heavy elements in the early stages. These heavy elements include condensable species such as H<sub>2</sub>O, NH<sub>3</sub>, and CH<sub>4</sub>, which are expected to have a great impact on atmospheric temperature and thus on radiative emission through latent heat release. In this study we investigate the effect of such condensation on the planetary emission flux and quantify the impact on the cooling timescale. We then demonstrate that the latent heat of these species keeps the atmosphere hot and thus the emission flux high for billions of years, resulting in an acceleration of the cooling of ice giants. This sheds light on the long-standing problem that Uranus is much less bright than theoretically predicted and is different in brightness from Neptune in spite of the similarity in mass and radius. We also find that young ice giants with highly enriched atmospheres are much brighter in the mid-infrared than ice giants with non-enriched atmospheres. This provides important implications for future direct imaging of extrasolar ice giants.

**Key words:** planets and satellites: atmospheres – planets and satellites: interiors

## 1. Introduction

The infrared brightness of giant planets is often used to understand how these planets formed and evolved to their present states and what has happened in their interior. During the formation, giant planets gain huge amounts of gravitational energy and then evolve by losing it into space via radiative emission. Thus, giant planets are initially hot, bright, and large, and subsequently become cool, dark, and small. By comparing the observed amount of infrared emission (hereafter the infrared luminosity) with the theoretical luminosity that one obtains by integrating planetary thermal evolution over the age, one sometimes realizes that the theoretical model includes some incorrect assumptions, which result in new findings.

The solar system gas giants Jupiter and Saturn have been relatively well investigated. The first theoretical model of Jupiter's thermal evolution (Hubbard 1977), which assumed a wholly convective and compositionally homogeneous interior, successfully yielded the infrared luminosity (or effective temperature) and radius, which were consistent with their observed values. When the same model is applied to Saturn, however, one obtains a luminosity that is much lower than observed. This discrepancy between theory and observation led to the finding that helium is immiscible with hydrogen and settles down under high pressure in Saturn's interior (Fortney & Nettelmann 2010, and references therein).

Moreover, recent observations have measured infrared luminosities of extrasolar gas giants (e.g., Marley et al. 2007; Kuzuhara et al. 2013). Because such exoplanets are detected by direct imaging, their masses are not measured but are constrained by comparison between observed and theoretical luminosities, unlike for solar system planets. Through

such studies regarding self-luminous gas giants, we have learned that it is crucial to understand thermal evolution of planets precisely to clarify their origin and properties.

In this study, our focus is on ice giants. The solar system ice giants Uranus and Neptune are quite similar in mass and radius with each other, indicating that they have almost the same bulk composition. Nevertheless, Uranus is fainter in the infrared by a factor of more than 10 than Neptune (Pearl et al. 1990). Furthermore, the faintness of Uranus is in itself puzzling: theoretical evolution models with the assumption of a chemically homogeneous, wholly convective interior predict that Uranus is currently much brighter in the infrared than observed (e.g., Hubbard & Macfarlane 1980; Fortney et al. 2011; Nettelmann et al. 2016). These problems have remained unsolved for more than 30 years (see Section 4.1 for details). Outside the solar system, Neptune-class planets are quite common according to recent exoplanet statistics (e.g., Batalha et al. 2013). Understanding the formation processes of these planets therefore is a major issue in astronomy and planetary science. Regarding Neptune-class exoplanets, while infrared direct imaging has not yet been successful, future telescopes (e.g., WFIRST-AFT, Spergel et al. 2015) are expected to detect infrared emission of cool exoplanets like the ice giants in the solar system. To derive planetary properties from such observations, we need accurate knowledge of the evolution of ice giants.

Theoretical models of the thermal evolution of ice giants so far assume that the material distribution in the interior and atmosphere is unchanged from birth until the present. Recent theories of planet formation, however, suggest that the interior and atmosphere are more mixed in the formation stage. For

example, small-sized bodies such as pebbles and collisional fragments may contribute to the accretion of ice giant cores (Inaba et al. 2003; Kobayashi et al. 2011; Lambrechts & Johansen 2014). Such small bodies are evaporated in the envelopes and may accelerate the formation of giant planets (Hori & Ikoma 2011; Venturini et al. 2015). Neptune-sized planets are also likely to experience giant collisions with protoplanets (Slattery 1992), which would modify the internal compositional distribution greatly. Since ice giants have large amounts of icy components such as  $\text{H}_2\text{O}$ ,  $\text{NH}_3$ , and  $\text{CH}_4$  in the interior, these icy components in the interior can be redistributed to the atmosphere by giant impacts.

This study is aimed to quantify the effect of icy-component enrichment in the atmosphere on the thermal evolution of ice giants. We assume that the ice giant initially possesses a significant amount of icy components in the atmosphere. Because of their latent heat, condensation of these components is expected to affect the temperature gradient in the convective region of the atmosphere and raises the atmospheric temperature compared to the temperature determined by dry adiabat. Here we demonstrate that such a change in atmospheric temperature significantly accelerates the cooling of ice giants.

Condensation of the icy components may prevent convection in the hydrogen-dominated atmospheres like those of ice giants. This is because these condensable molecules are all heavier than hydrogen, so that condensation yields a mean molecular weight gradient in the atmosphere. This, however, remains a controversial issue. According to Guillot (1995) and Leconte et al. (2016), the mixing ratios of  $\text{CH}_4$  in the atmospheres of Uranus and Neptune are higher than the threshold values beyond which convection is inhibited, but  $\text{CH}_4$  clouds, which form via convective motion, are observed in the atmospheres (Lindal et al. 1987; Orton et al. 2014a, 2014b).

The rest of this paper is organized as follows. In Section 2 we describe our theoretical models and calculation methods of the atmosphere and interior structures and thermal evolution of ice giants. In Section 3 we show our calculation results, in particular, the effects of latent heat of icy components on the atmospheric structure and thermal evolution of the ice giant. Then, in Section 4, we discuss the implication for the faint Uranus paradox (Section 4.1) and the detectability of young exo-Neptunes (Section 4.2) by applying our new evolution models. We also discuss caveats of our evolution model, including inhibition of convection caused by possible meanmolecular weight gradients and resulting layered convection (Section 4.3). Last, we summarize and conclude this paper in Section 5.

## 2. Model Description

In this study, we numerically integrate the thermal evolution of an ice giant, including the effect of condensation in its atmosphere. We assume that the planet consists of four layers in spherical symmetry and hydrostatic equilibrium, which include, from top to bottom, (1) an atmosphere composed of hydrogen, helium, water, ammonia, and methane, (2) an envelope composed of hydrogen, helium, and water, (3) a water-ice mantle, and (4) a rocky core. At each interface, the pressure and temperature are continuous. We sometimes refer to the last three layers collectively as the interior, hereafter. Each layer in the interior is assumed to be fully convective and isentropic, and uniform in elemental abundance.

### 2.1. Interior Structure

The structure of the interior is determined by the differential equations

$$\frac{\partial P}{\partial M_r} = -\frac{GM_r}{4\pi r^4}, \quad (1)$$

$$\frac{\partial r}{\partial M_r} = \frac{1}{4\pi r^2 \rho}, \quad (2)$$

$$\frac{\partial T}{\partial M_r} = -\frac{GM_r}{4\pi r^4} \frac{T}{P} \nabla, \quad (3)$$

and the equation of state,

$$\rho = \rho(P, T, X_i), \quad (4)$$

where  $r$  is the planetocentric distance,  $M_r$  is the mass contained in the sphere of radius  $r$ ,  $P$  is the pressure,  $\rho$  is the density,  $T$  is the temperature,  $X_i$  symbolically denotes the composition, and  $G$  is the gravitational constant ( $=6.67 \times 10^{-8} \text{ dyn cm}^2 \text{ g}^{-2}$ ). The symbol  $\nabla$  is the adiabatic temperature gradient with respect to pressure, namely,

$$\nabla = \nabla_{\text{ad}} = \left( \frac{\partial \ln T}{\partial \ln P} \right)_s. \quad (5)$$

As for the equations of state, we use Saumon et al. (1995) for hydrogen and helium, SESAME 7150 for water (Lyon & Johnson 1992), and Valencia et al. (2007) for rock. For the mixing of hydrogen, helium, and water in the envelope, we adopt the volume-additive law (Saumon et al. 1995),

$$\frac{1}{\rho} = (1 - Z_0) \left( \frac{X}{\rho_{\text{H}}} + \frac{Y}{\rho_{\text{He}}} \right) + \frac{Z_0}{\rho_{\text{H}_2\text{O}}}, \quad (6)$$

where  $X$ ,  $Y$ , and  $Z_0$  are the mass fractions of hydrogen, helium, and water, respectively, and  $\rho_{\text{H}}$ ,  $\rho_{\text{He}}$ , and  $\rho_{\text{H}_2\text{O}}$  are the partial densities of hydrogen, helium, and water, respectively. We set  $X = 0.72$  and  $Y = 0.28$ , which are the protosolar mass fractions without the heavy elements (Lodders et al. 2009). Since the behavior of ammonia and methane at high pressures and high temperatures is poorly known, we substitute the equation of state of water for those of ammonia and methane in accordance with previous research (e.g., Nettelmann et al. 2013). In this study, we deal with  $Z_0$  as the sum of the fractions of water, ammonia, and methane.

### 2.2. Atmospheric Structure

The atmosphere is assumed to be plane parallel and in radiative-convective equilibrium. Thus, the net flux is constant throughout the atmosphere. The atmosphere contains  $\text{H}_2$ ,  $\text{He}$ ,  $\text{H}_2\text{O}$ ,  $\text{NH}_3$ , and  $\text{CH}_4$  gases and  $\text{H}_2\text{O}$ ,  $\text{NH}_3$ , and  $\text{CH}_4$  condensates (hereafter,  $\text{H}_2\text{O}$ ,  $\text{NH}_3$ , and  $\text{CH}_4$  are referred to collectively as the volatile). The distribution of each volatile component is determined by the phase equilibrium condition (i.e., saturation pressure). The interface between the atmosphere and interior (i.e., the bottom of the atmosphere) is assumed to be at a pressure level of 100 bar, which is denoted by  $P_{\text{btm}}$ . The transition pressure  $P_{\text{btm}}$  must be high enough for condensation to occur in the atmosphere, not in the interior. On the other hand, since we assume that the mass of the atmosphere is negligibly small, the transition pressure must be low enough. We have chosen the value of 100 bar because this

value fulfills these conditions. The choice of transition pressure scarcely affects the results and conclusions given below as long as these assumptions are valid.

The temperature-pressure relation in the radiative region (or stratosphere) is determined by the analytical formula derived by Matsui & Abe (1986):

$$\sigma T^4 = F_{\text{top}} \frac{\tau + 1}{2} + \frac{\sigma T_{\text{eq}}^4}{2} \left[ 1 + \frac{\kappa_{\text{th}}}{\kappa_{\text{v}}} + \left( \frac{\kappa_{\text{v}}}{\kappa_{\text{th}}} - \frac{\kappa_{\text{th}}}{\kappa_{\text{v}}} \right) \exp^{-\tau_{\text{v}}} \right], \quad (7)$$

where  $F_{\text{top}}$  is the net flux,  $T_{\text{eq}}$  is the equilibrium temperature,  $\kappa_{\text{th}}$  and  $\kappa_{\text{v}}$  are the mean opacities for long- and short-wavelength radiation, respectively,  $\tau$  and  $\tau_{\text{v}}$  are the optical depths for long- and short-wavelength radiation, respectively, and  $\sigma$  is the Stefan-Boltzmann constant ( $=5.67 \times 10^{-5} \text{ erg cm}^{-2} \text{ K}^{-4} \text{ s}^{-1}$ ). The optical depth  $\tau$  is defined as  $d\tau = -\rho \kappa_{\text{th}} dr$ .

We assume that  $\kappa_{\text{th}}$  is the Rosseland mean opacity and  $\kappa_{\text{v}} = 0.1\kappa_{\text{th}}$ . This assumption is verified by comparison between the above analytical formula and  $T$ - $P$  profiles obtained from detailed radiative transfer calculations for hot-Jupiter atmospheres (Guillot 2010). We also neglect the short-wavelength radiation reflectivity and assume that the single scattering albedo is unity. By comparing our atmospheric model with that including the effects of short-wavelength stellar irradiation in detail (Marley & McKay 1999), we have confirmed that short-wavelength radiation has little influence on the temperature-pressure structure of  $\tau > 1$ , which is of special interest in this study. The opacities of  $\text{H}_2$  and  $\text{He}$  are due to collision-induced absorption and Rayleigh scattering, for which we have used the data table from Freedman et al. (2008): the data are available for densities  $\rho = 2.5 \times 10^{-12}$  to  $10 \text{ g cm}^{-3}$  and temperatures  $T = 10^2$  to  $10^4 \text{ K}$ . The opacities of  $\text{H}_2\text{O}$ ,  $\text{NH}_3$ , and  $\text{CH}_4$  gases are calculated from line profiles derived from the HITRAN 2012 database (Rothman et al. 2013). The calculation method of the line profiles is based on Rothman et al. (1998). We adopt the Voigt profile as the line shape and use the analytical formula that Kuntz (1997) derived by implementing Humlices's algorithm for approximation. Kuntz (1997) showed that the implementation of Humlicek's algorithm yields errors of at most  $2 \times 10^{-6}$ , which stems from the cutoff for the Voigt function. The monochromatic opacity  $\kappa(\nu)$  is calculated as

$$\kappa(\nu) = \frac{k_{\eta\eta'}(\nu, T, P)}{M}, \quad (8)$$

where  $M$  is the mass of the molecule and  $k_{\eta\eta'}$  is the monochromatic absorption coefficient for the transition between lower  $\eta$  and upper  $\eta'$  states. We obtain the Rosseland mean opacities of  $\text{H}_2$  ( $\kappa_{\text{H}_2}$ ),  $\text{He}$  ( $\kappa_{\text{He}}$ ),  $\text{H}_2\text{O}$  ( $\kappa_{\text{H}_2\text{O}}$ ),  $\text{NH}_3$  ( $\kappa_{\text{NH}_3}$ ), and  $\text{CH}_4$  ( $\kappa_{\text{CH}_4}$ ) molecules from line intensities. Then, we calculate the total opacity  $\kappa_{\text{th}}$  as

$$\kappa_{\text{th}} = x_{\text{H}_2} \kappa_{\text{H}_2} + x_{\text{He}} \kappa_{\text{He}} + x_{\text{H}_2\text{O}} \kappa_{\text{H}_2\text{O}} + x_{\text{NH}_3} \kappa_{\text{NH}_3} + x_{\text{CH}_4} \kappa_{\text{CH}_4}, \quad (9)$$

where  $x_{\text{H}_2}$ ,  $x_{\text{He}}$ ,  $x_{\text{H}_2\text{O}}$ ,  $x_{\text{NH}_3}$ , and  $x_{\text{CH}_4}$  are the mole fractions of  $\text{H}_2$ ,  $\text{He}$ ,  $\text{H}_2\text{O}$ ,  $\text{NH}_3$ , and  $\text{CH}_4$ , respectively.

The temperature gradient in the convective region (or troposphere) is determined by the pseudo-moist adiabatic gradient. For  $N$  kinds of species including  $j$  kinds of non-condensable species,

the pseudo-moist adiabatic temperature gradient is given by (Ingersoll 1969; Atreya 1986; Abe & Matsui 1988)

$$\frac{d \ln T}{d \ln P} = \nabla_{\text{dry}} \frac{1 + \sum_{i=j+1}^N \frac{x_i}{1-x_i} \frac{d \ln p_i^*}{d \ln T}}{1 + \sum_{i=j+1}^N \frac{R_g}{C_p} \frac{x_i}{1-x_i} \frac{d \ln p_i^*}{d \ln T}}, \quad (10)$$

where  $\nabla_{\text{dry}}$  is the adiabatic temperature gradient without condensation (i.e., dry adiabatic),  $C_p = \sum_{i=1}^N x_i C_{p,i}$  is the mean heat capacity,  $x_i$  and  $p_i^*$  are the mole fraction and vapor pressure of condensable species  $i$  ( $i = j+1, \dots, N$ ). The vapor pressure of  $\text{H}_2\text{O}$  and the pressures of  $\text{NH}_3$  and  $\text{CH}_4$  are taken from Nakajima et al. (1992) and Sánchez-Lavega et al. (2004), respectively. We assume that the heat capacities of  $\text{H}_2\text{O}$ ,  $\text{NH}_3$ , and  $\text{CH}_4$  at constant pressure are  $4 R_g$ , where  $R_g$  is the gas constant, as an ideal gas approximation. The atmospheric temperature of interest in this study is lower than 500 K for  $\text{H}_2\text{O}$  and lower than 300 K for  $\text{NH}_3$  and  $\text{CH}_4$ . In this temperature range, the assumption for the heat capacity is in good agreement with experiments. We ignore the non-ideal effect of the condensates because it is negligible at the height of  $\tau \sim 1$ , where the radiation from the top of the atmosphere is determined.

We integrate the radiation transfer equation by using the Eddington approximation. The upward and downward radiation flux densities  $F_{\text{IR}}^+$  and  $F_{\text{IR}}^-$  can be written as

$$F_{\text{IR}}^+(\tau) = \pi B(\tau) - \int_{\tau_b}^{\tau} \frac{d}{d\tau'} (\pi B(\tau')) \exp\left(-\frac{3}{2}(\tau' - \tau)\right) d\tau', \quad (11)$$

$$F_{\text{IR}}^-(\tau) = \pi B(\tau) - \int_0^{\tau} \frac{d}{d\tau'} (\pi B(\tau')) \exp\left(-\frac{3}{2}(\tau - \tau')\right) d\tau' - \pi B(0) \exp\left(-\frac{3}{2}\tau\right), \quad (12)$$

the net radiative flux as

$$F_{\text{rad}} = F_{\text{IR}}^+ - F_{\text{IR}}^- - F_{\text{irr}}, \quad (13)$$

and the net flux as

$$F_{\text{net}} = F_{\text{rad}} + F_c, \quad (14)$$

where  $B(\tau)$  is the blackbody radiation intensity,  $F_c$  is the convective flux, and  $F_{\text{irr}}$  is the direct solar flux. Note that  $F_{\text{top}} = F_{\text{IR}}^+(\tau = 0)$ . We assume the net flux is constant throughout the atmosphere and that the convective flux is equal to zero in the stratosphere.

### 2.3. Thermal Evolution

To simulate the thermal evolution, we integrate the energy conservation equation,

$$\frac{\partial L_r}{\partial M_r} = -T \frac{dS}{dt}, \quad (15)$$

where  $S$  is the specific entropy,  $L_r$  is the total energy flux passing through a sphere of radius  $r$ , and  $t$  is time. Integrating the equation from the center to the top, we obtain the intrinsic

luminosity  $L_{\text{int}}$  as

$$L_{\text{int}} = - \left[ \frac{dS_{\text{env}}}{dt} \int_{M_c+M_m}^{M_p} T dM_r + \frac{dS_m}{dt} \int_{M_c}^{M_c+M_m} T dM_r + \frac{dS_c}{dt} \int_0^{M_c} T dM_r \right], \quad (16)$$

where  $S_{\text{env}}$ ,  $S_m$ , and  $S_c$  are the specific entropies of the envelope, the mantle, and the core, respectively, and  $M_c$  and  $M_m$  are the masses of the core and mantle, respectively.  $L_{\text{int}}$  is also written as  $L_{\text{int}} = 4\pi R_p^2 F_{\text{top}}$ , where  $R_p$  is the planetary radius and  $F_{\text{top}}$  is the outgoing flux from the top of the atmosphere.

#### 2.4. Numerical Procedure

Numerically, we integrate Equation (16) by the following procedure. First, we determine the atmospheric structure and the intrinsic luminosity  $L_{\text{int}}$ , which correspond to the outer boundary conditions for the interior structure. To do so, assuming trial values of  $F_{\text{top}}$  and the pressure  $P_{\text{ad}}$  at the boundary between the stratosphere and the troposphere, which we call the tropopause pressure, we calculate the  $T$ - $P$  profile in the stratosphere from Equation (7) and that in the troposphere from Equation (10). From these profiles, we calculate the upward and downward fluxes from Equations (11)–(14). The tropopause pressure  $P_{\text{ad}}$  is determined by the divergence of the net flux for radiation. That is, in the troposphere, the net flux satisfies

$$\frac{dF_{\text{rad}}}{d\tau} \sim \frac{F_{\text{rad}}^{i+1} - F_{\text{rad}}^i}{\tau_{i+1} - \tau_i} < 0, \quad (17)$$

while in the stratosphere,

$$\frac{dF_{\text{rad}}}{d\tau} \sim \frac{F_{\text{rad}}^{i+1} - F_{\text{rad}}^i}{\tau_{i+1} - \tau_i} \geq 0, \quad (18)$$

where  $i$  is the grid number. We assume that the top of the atmosphere is  $P_{\text{top}} = 1 \times 10^{-5}$  bar. If the tropospheric temperature derived by Equation (7) is lower (higher) than that derived by Equation (10), the trial value of  $P_{\text{ad}}$  is higher (smaller) than the actual value. Then, we set the value of  $P_{\text{ad}}$  for the next step smaller (higher). We also replace the value of  $F_{\text{top}}$  with the value calculated by Equation (11). We repeat this procedure until we obtain the self-consistent values of  $P_{\text{ad}}$  and  $F_{\text{top}}$  that satisfies the relative error of temperature at the tropopause lower than 1%. At this point, we determine the temperature at  $P = P_{\text{btm}}$  (denoted by  $T_{\text{btm}}$ ) from which we calculate the specific entropy of the envelope.

We determine the masses of the rocky core ( $M_c$ ), the water mantle ( $M_m$ ), and the envelope ( $M_e$ ) from the total mass fractions of heavy elements in the interior ( $Z_{\text{tot}}$ ) and in the envelope ( $Z_0$ ), and the water mass fraction in the interior ( $Z_w$ ), which are respectively defined as

$$Z_{\text{tot}} = \frac{M_{e,w} + M_m + M_c}{M_p}, \quad (19)$$

$$Z_0 = \frac{M_{e,w}}{M_e}, \quad (20)$$

$$Z_w = \frac{M_{e,w} + M_m}{M_p}, \quad (21)$$

where  $M_{e,w}$  is the total mass of water in the envelope. That is, we calculate the mass fractions of the core, mantle, and envelope as

$$\frac{M_c}{M_p} = (1 - Z_w) \cdot Z_{\text{tot}}, \quad (22)$$

$$\frac{M_m}{M_p} = Z_w \cdot Z_{\text{tot}} - \frac{Z_0(1 - Z_{\text{tot}})}{1 - Z_0}, \quad (23)$$

$$\frac{M_e}{M_p} = 1 - Z_{\text{tot}} + \frac{Z_0(1 - Z_{\text{tot}})}{1 - Z_0}, \quad (24)$$

respectively.

Finally, Equation (16) is numerically integrated in the following way. For each time step, we first simulate two interior models for two different values of  $T_{\text{btm}}$ . We integrate Equations (1)–(4) inward from the atmospheric bottom,  $M_r = M_p$  (neglecting the mass of the atmosphere), to the planetary center,  $M_r = 0$ , using the fourth-order Runge-Kutta method. We then look for the solution that fulfills the inner boundary condition (i.e.,  $r=0$  at  $M_r=0$ ) in an iterative fashion, by changing the planetary radius ( $R_p$ ). Note that determining  $P_{\text{ad}}$  and  $F_{\text{top}}$  requires the gravity in the atmosphere (or the planetary radius  $R_p$ ), which is obtained after the interior structure is determined. Thus, we have to find the solution in which the interior and atmospheric structures are consistent with each other also in an iterative fashion. Then we calculate the time interval  $\Delta t$  from the second-order difference equation for Equation (16), which is written as

$$\Delta t = - \frac{C}{L_{\text{int}}(t + \Delta t) + L_{\text{int}}(t)}, \quad (25)$$

where

$$C = [S_{\text{env}}(t + \Delta t) - S_e(t)][\Theta_{\text{env}}(t + \Delta t) + \Theta_{\text{env}}(t)] \\ + [S_m(t + \Delta t) - S_m(t)][\Theta_m(t + \Delta t) + \Theta_m(t)] \\ + [S_c(t + \Delta t) - S_c(t)][\Theta_c(t + \Delta t) + \Theta_c(t)], \quad (26)$$

and

$$\Theta_{\text{env}}(t) \equiv \int_{M_m+M_c}^{M_p} T(t) dM_r, \quad (27)$$

$$\Theta_m(t) \equiv \int_{M_c}^{M_m+M_c} T(t) dM_r, \quad (28)$$

$$\Theta_c(t) \equiv \int_0^{M_c} T(t) dM_r, \quad (29)$$

and  $S_{\text{env}}$ ,  $S_m$ , and  $S_c$  are the entropies of the envelope, the mantle, and the core, respectively. We have confirmed that our numerical code for the atmospheric structure reproduces the  $P_{\text{ad}}$  and  $F_{\text{top}}$  values presented by Nakajima et al. (1992) well. We have also confirmed that our numerical code for the interior structure reproduces the mass and radius relationship for super-Earths presented by Valencia et al. (2010) well.

The free parameters in this model are the total mole fraction of the volatiles (i.e.,  $\text{H}_2\text{O}$ ,  $\text{NH}_3$ , and  $\text{CH}_4$ ) in the atmosphere  $x_{\text{btm}}(t = 0)$ , the initial mole ratios of  $\text{NH}_3/\text{H}_2\text{O}$  and  $\text{CH}_4/(\text{H}_2+\text{He})$  at the atmospheric bottom, the abundance of helium with respect to hydrogen ( $Y$ ), the pressure at the atmospheric



**Table 1**  
Parameters Used in the Fiducial Result

$M_p$ (g)	$T_{eq}$ (K)	$Z_w$	$Z_{tot}$
$8.68 \times 10^{28}$	58.2	0.95	0.90
$P_{btm}$ [bar]	$x_{btm}$ [mol%]	$NH_3/H_2O$	$CH_4/(H_2+He)$
100	2.3–50	0.135	0.023

bottom  $P_{btm}$ , the total heavy element mass fraction of the planet  $Z_{tot}$ , and the total mass fraction of heavy elements in the envelope  $Z_0$ . In this study, we assume  $Z_w = 0.95$ . The conversion relation between  $x_{btm}$  and  $Z_0$  is

$$x_{btm} = \frac{Z_0}{\frac{\mu_w}{\mu_H}(1 - Z_0) + Z_0}, \quad (30)$$

where  $\mu_w$  and  $\mu_H$  are the molecular weights of  $H_2O$  (=18.0) and of the mixture of  $H_2$  and  $He$  with solar abundances (=2.3), respectively. We assume that the abundance of water in the envelope is constant throughout the evolution. We also assume the initial mole ratios of  $NH_3/H_2O = 0.135$ , which is equal to the N/O value of the solar abundance (Lodders et al. 2009), and the mole fraction of  $CH_4/(H_2+He) = 0.023$ , which is the present  $CH_4$  mixing ratio of the atmosphere of Uranus (Lindal et al. 1987; Marley & McKay 1999). Table 1 summarizes the parameters and their fiducial values.

Finally, since the atmosphere that is cold enough for the volatiles to condense is of interest in this study, we adopt the Uranus value (58.2 K) for  $T_{eq}$ . The incident solar radiation flux ( $L_{eq}$ ) is calculated by  $L_{eq} = 4\pi R_p^2 \sigma T_{eq}^4$ . We also assume that the planetary mass is Uranus' mass ( $=8.68 \times 10^{28}$  g).

### 3. Results

#### 3.1. Atmospheric Structure

First we investigate the effect of condensation on the atmospheric structure. Figure 1 shows  $T$ - $P$  profiles in the atmosphere for various values of  $T_{btm}$ . We set the mole fractions of  $H_2 + He$ ,  $H_2O$ ,  $NH_3$ , and  $CH_4$  at 50.0%, 43.0%, 5.80%, and 1.18%, respectively. The atmospheric structure is composed of three parts, a dry convective region, a moist convective region, and a radiative region (i.e., a stratosphere) from the bottom to the top. The temperature gradient in the dry convective region is determined by the heat capacity of the dominant constituents, whereas it is controlled by the latent heat of the condensable constituents in the moist convective region. The green lines in Figure 1 represent the case where the main condensed constituent is  $H_2O$ . As  $T_{btm}$  decreases, the  $T$ - $P$  curve shifts from right to left. In Figure 1, the shift does not occur uniformly. In the lower atmosphere, the temperature at a given pressure changes with  $T_{btm}$ , whereas it is almost unchanged in the middle and upper atmosphere. This is because condensation of  $H_2O$  occurs in the middle atmosphere, so that the  $T$ - $P$  curve is fixed to the saturation  $T$ - $P$  relation (i.e., vapor pressure). Once almost all water is depleted by precipitation, the  $T$ - $P$  profile moves leftward as a whole. Then, the next condensate (i.e.,  $NH_3$  and  $CH_4$  in the blue line and black line cases, respectively) determines the  $T$ - $P$  profile in the middle atmosphere.

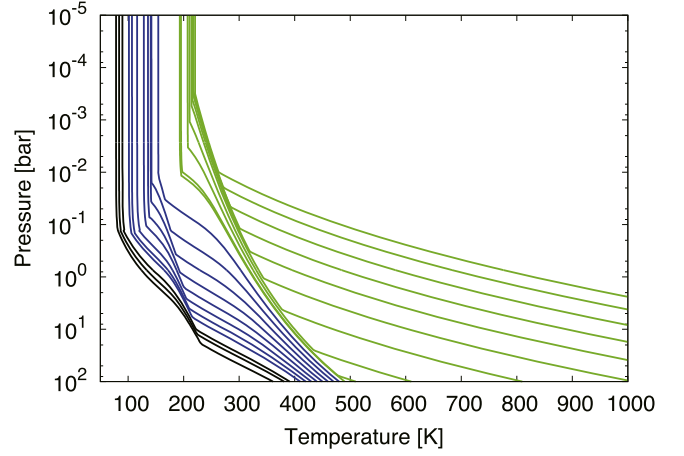


**Figure 1.** Temperature-pressure profiles in the atmosphere for different values of the temperature at 100 bar,  $T_{btm}$ . The atmosphere consists of  $H_2$ ,  $He$ ,  $H_2O$ ,  $NH_3$ , and  $CH_4$ , the mole fractions of which are 45.6%, 4.42%, 43.0%, 5.80%, and 1.18%, respectively. Condensation of  $H_2O$ ,  $NH_3$ , and  $CH_4$  are taken into account. The green, blue, and black lines represent the cases where the main condensate is  $H_2O$ ,  $NH_3$ , and  $CH_4$ , respectively. The equilibrium temperature is assumed to be 58.2 K.

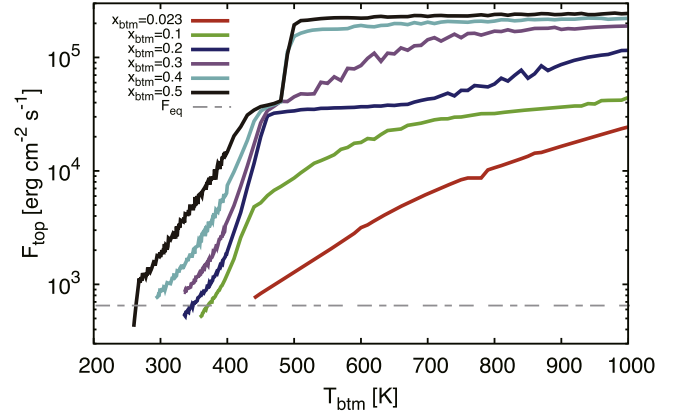


**Figure 2.** Calculated relationship between the outgoing radiative flux at the top of the atmosphere  $F_{top}$  and the temperature at 100 bar in the atmosphere  $T_{btm}$  for six different values of the total mole fraction of the volatiles (i.e.,  $H_2O$ ,  $NH_3$ , and  $CH_4$ )  $x_{btm} = 0.023$  (red), 0.1 (green), 0.2 (blue), 0.3 (purple), 0.4 (cyan), and 0.5 (black). The horizontal thin black line represents the equilibrium flux  $\sigma T_{eq}^4$ . Here we have assumed the mole fraction of  $CH_4/H_2 = 0.023$  and  $NH_3/H_2O = 0.135$ , and the equilibrium temperature is 58.2 K.

Figure 2 shows the outgoing flux from the top of the atmosphere  $F_{top}$  as a function of  $T_{btm}$  for different values of the total mole fraction of the volatiles  $x_{btm}$ . To see the condensation effect on the outgoing flux, we first focus on the result for  $x_{btm} = 0.5$  (black line). For  $T_{btm} \gtrsim 500$  K,  $F_{top}$  is nearly constant ( $=3.3 \times 10^5$  erg s $^{-1}$  cm $^{-2}$ ). This value is similar to the Komabayashi-Ingersoll limit of  $H_2O$  dominated atmospheres (Nakajima et al. 1992). That is because the atmospheric temperature structure is determined by the moist convection of  $H_2O$ , as described above. Moreover, the surface of  $\tau \simeq 1$ , which we call hereafter the atmospheric photosphere, is in the moist convective region. Therefore  $F_{top}$  is nearly constant in the temperature range where the atmospheric structure is dominated by the moist convection of  $H_2O$ . Hereafter we call this constant  $F_{top}$  the radiation limit.

The radiation limit also appears when condensation of  $NH_3$  or  $CH_4$  occurs. The flux  $F_{top}$  changes sharply at  $T_{btm} \simeq 500$  K.

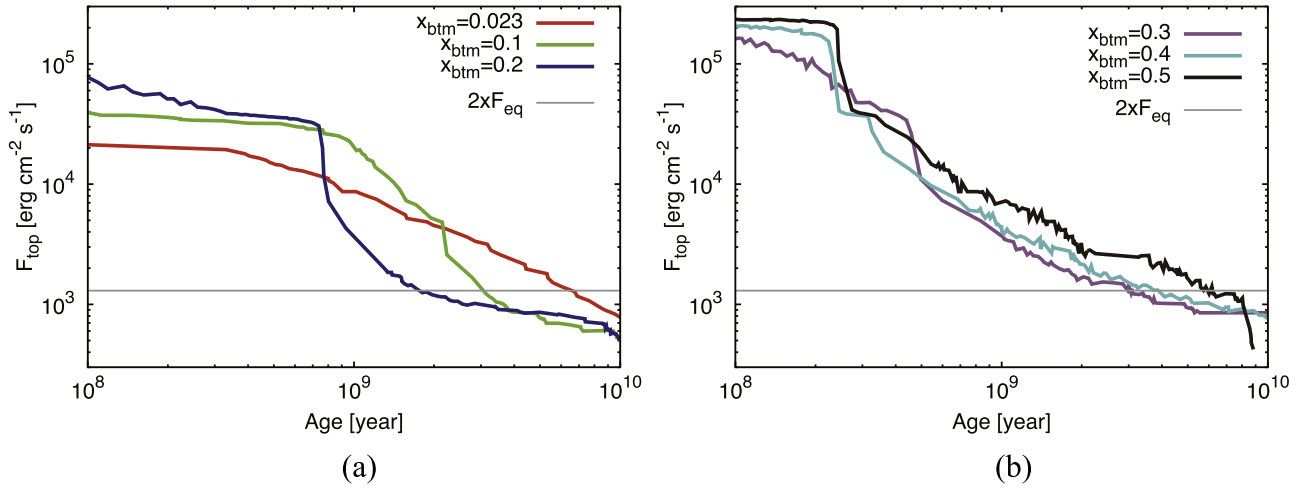


**Figure 3.** Evolution of the outgoing flux at the top of the atmosphere  $F_{\text{top}}$  for different values of the initial total mole fraction of the volatiles ( $\text{H}_2\text{O}+\text{NH}_3+\text{CH}_4$ ) in the atmosphere. Panels (a) and (b) show the results for  $x_{\text{btm}} = 0.023$  (red), 0.1 (green), and 0.2 (blue) and those for  $x_{\text{btm}} = 0.3$  (purple), 0.4 (cyan), and 0.5 (black), respectively. Here we have assumed that the equilibrium temperature  $T_{\text{eq}}$  is 58.2 K. The gray line represents twice the incident stellar radiative flux,  $F_{\text{eq}}$  (i.e.,  $2\sigma T_{\text{eq}}^4$ ). The values of the other parameters used are listed in Table 1.

Once  $T_{\text{btm}}$  reaches about 450 K,  $F_{\text{top}}$  settles down to the radiation limit due to  $\text{NH}_3$  condensation ( $\sim 3 \times 10^4 \text{ erg s}^{-1} \text{ cm}^{-2}$ ).  $F_{\text{top}}$  decreases only slightly in the range of  $T_{\text{btm}} \simeq 420\text{--}450$  K because of  $\text{NH}_3$  condensation, and then decreases rapidly for  $T_{\text{btm}} \lesssim 420$  K after  $\text{NH}_3$  is depleted. In the case of small  $x_{\text{btm}}$ , the domain of slow change around  $T_{\text{btm}} \simeq 400$  K disappears because of the low abundance of  $\text{NH}_3$ .

Finally, for  $T_{\text{btm}} \lesssim 250$  K, the atmospheric structure is affected by  $\text{CH}_4$  condensation. However, since  $\text{CH}_4$  is not abundant enough for its latent heat to dominate the structure,  $F_{\text{top}}$  is not constant but decreases as  $T_{\text{btm}}$  decreases.

As  $x_{\text{btm}}$  decreases,  $F_{\text{top}}$  decreases for a given  $T_{\text{btm}}$ . This is because the contribution of latent heat to heat capacity becomes small with decreasing  $x_{\text{btm}}$ , so that the photospheric temperature decreases. Indeed, in the case of dry convection ( $x_{\text{btm}} = 0.023$ ; red line),  $F_{\text{top}}$  is considerably small relative to, for example, that for  $x_{\text{btm}} = 0.5$  (black line). Furthermore, because of the low abundances of the condensable molecules, the domains of constant  $F_{\text{top}}$  disappear in cases of low  $x_{\text{btm}}$ .

### 3.2. Thermal Evolution

Here we investigate the thermal evolution of ice giants with volatile-rich atmospheres. Figure 3 shows the evolution of  $F_{\text{top}}$  for different values of  $x_{\text{btm}}$ . The evolution of the planetary radius  $R_p$  is also shown in Figure 4. As seen in Figure 3, the planet with an atmosphere richer in the volatiles is more luminous in early stages. This is because the stratospheric temperature is kept high because of the release of latent heat in the troposphere (Figures 1 and 2). If the atmosphere is more enriched initially,  $F_{\text{top}}$  is larger and the cooling occurs more rapidly, so that the effective temperature reaches the equilibrium value earlier. For example,  $F_{\text{top}}$  reaches  $2 \times F_{\text{eq}}$  within  $4 \times 10^9$  years if  $x_{\text{btm}} = 0.1$  to 0.4, whereas it takes  $7 \times 10^9$  years if  $x_{\text{btm}} = 0.023$ . This is because, as shown in Figure 2, larger  $x_{\text{btm}}$  causes larger  $F_{\text{top}}$ , leading to rapid cooling of the planet. However,  $F_{\text{top}}$  for  $x_{\text{btm}} = 0.5$  is larger than that for  $x_{\text{btm}} \leq 0.4$  at  $t > 4$  Gyr. That is because the condensation of  $\text{CH}_4$  dominates the planetary flux in the case of  $x_{\text{btm}} = 0.5$ .

Figure 4 shows the evolution of the planetary radius for the same parameter values as those used in Figure 3. The larger

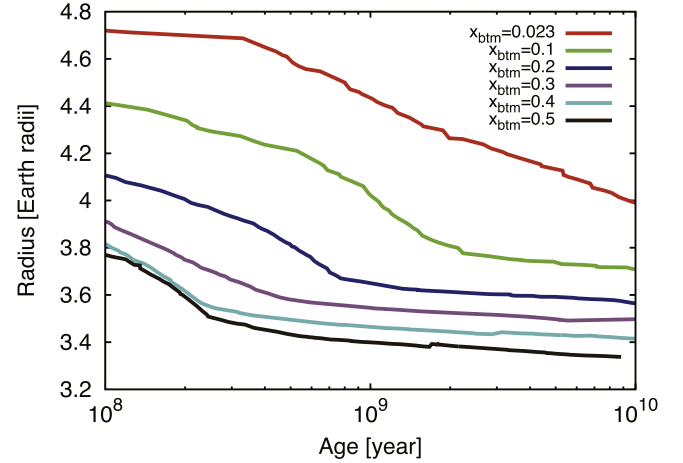


**Figure 4.** Evolution of the planetary radius. Lines are colored according to the initial total mole fraction of the volatile ( $\text{H}_2\text{O}+\text{NH}_3+\text{CH}_4$ ) in the atmosphere,  $x_{\text{btm}} = 0.023$  (red), 0.1 (green), 0.2 (blue), 0.3 (purple), 0.4 (cyan), and 0.5 (black). Parameter values used for these calculations are the same as those used in Figure 3.

$x_{\text{btm}}$ , the smaller the radius at a given age for two reasons: first, because large  $x_{\text{btm}}$  corresponds to heavy-element-rich interior (i.e., large  $Z_0$ ; see Equation (30)), the planet is small. Second, as seen in Figure 3, large  $x_{\text{btm}}$  results in rapid cooling of the planet, which leads to rapid contraction. Because of these two effects, the planet with a volatile-rich atmosphere is considerably smaller than that with a volatile-poor atmosphere.

## 4. Discussion

### 4.1. Faint Uranus Paradox

The faint Uranus paradox is a long-standing unsolved problem. As mentioned in the Introduction, Uranus is much darker in the infrared than theoretically predicted. More exactly, when we integrate the thermal evolution of Uranus backward from the present state, based on conventional models that assume that the material distribution in the interior and atmosphere has been the same as the present (Hubbard & Macfarlane 1980; Fortney et al. 2011), one obtains an initial

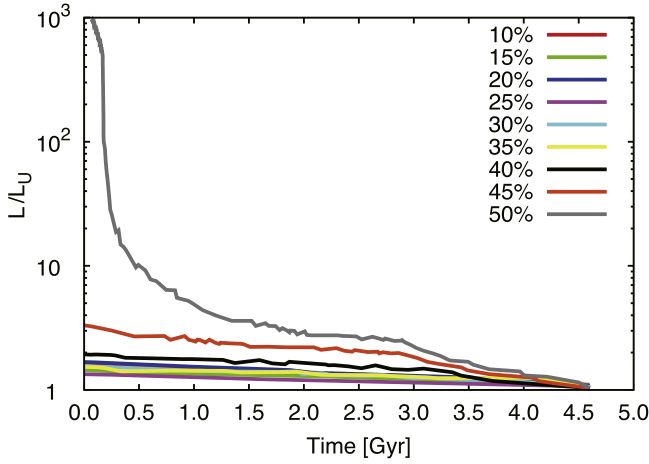


**Figure 5.** Evolution of the planetary luminosity  $L$  in the unit of the present luminosity of Uranus  $L_U$  ( $=5.6 \times 10^{22} \text{ erg s}^{-1}$ ). Lines are colored according to the total mole fraction of the volatiles (i.e.,  $\text{H}_2\text{O}$ ,  $\text{NH}_3$ , and  $\text{CH}_4$ ) in the atmosphere from 10-mol% to 50 mol%. We assume a total heavy element mass in the planet of  $Z_{\text{tot}} = 0.9$  and a mass fraction of water of  $Z_W = 0.95$ . The heavy element mass in the planetary envelope  $Z_0$  is determined by  $x_{\text{btm}}$  using Equation (30).  $Z_{\text{tot}}$ ,  $Z_W$ , and  $Z_0$  are constant throughout the evolution. The planetary mass is  $8.68 \times 10^{28} \text{ g}$ .

effective temperature of as low as 65–70 K. This temperature corresponds to a planet accretion timescale on the order of ten billion years, which means that Uranus’ formation timescale is much longer than the age of the solar system.

A few ideas have been proposed that heat transport is prevented in the interior for some reason, resulting in low emission. One possible mechanism is inefficient convection due to compositional gradient (Stevenson 1982; Podolak & Helled 2012), which causes the so-called double-diffusive convection. The double-diffusive convection, however, tends to disappear in about one billion years, and instead, overturning vigorous convection occurs in the interior (Kurokawa & Inutsuka 2015). Another possible mechanism is delay in cooling due to the presence of thermal boundary layers in the interior. For example, the transition region between the H/He-dominated envelope and the ice-dominated mantle is stably stratified and behaves as a thermal boundary layer. Nettelmann et al. (2016) demonstrated that the thermal boundary layer could work well to reproduce the low luminosity of Uranus. The problem remains, however, of why the same process does not occur in Neptune.

Here, applying our new evolution model, we propose a scenario that can explain the infrared darkness of Uranus and the difference from Neptune. In Figure 5 we show the thermal evolution models that we have obtained by integrating the evolution backward from the present (the present luminosity  $L_U$  is  $5.6 \times 10^{22} \text{ erg s}^{-1}$ ). The values of parameters other than  $x_{\text{btm}}$  are given in Table 1. Our calculation demonstrates that a planet with an atmosphere of  $x_{\text{btm}} = 50 \text{ mol\%}$  is quite luminous at  $t = 0$ . Namely, if Uranus’ atmosphere had been initially sufficiently polluted with condensable constituents, planetary cooling would have occurred rapidly enough to result in the present luminosity of Uranus within the age of the solar system.

The questions are what caused the atmospheric pollution and why such a process occurred only for Uranus. One possible process is giant impacts. Namely, a giant impact dredged up condensable constituents from the icy deep interior, distributing

them around the proto-Uranus to form a circumplanetary disk. Then the atmosphere became highly polluted by reaccrretion of the condensable constituents from the circumplanetary disk. This scenario would also be consistent with the highly inclined obliquity of Uranus ( $=97.77^\circ$ ), which can be explained by a giant impact event (Slattery 1992; Morbidelli et al. 2012). On the other hand, Neptune may not have experienced such a giant impact because of its low obliquity ( $=28.32^\circ$ ). If that were the case, Neptune would have initially had a less polluted, dry atmosphere, which would also explain the present luminosity of Neptune (Fortney et al. 2011; Nettelmann et al. 2013). Thus, giant impacts likely played a key role in creating the great difference in brightness between Uranus and Neptune.

However, the planetary radius that we have calculated here is smaller than the present radius of Uranus ( $=4.0 R_\oplus$ ). In the case of  $x_{\text{btm}} = 50 \text{ mol\%}$  ( $Z_0 = 0.887$ ), the calculated present planetary radius is  $3.4 R_\oplus$ . In order to produce both a planetary radius and an intrinsic luminosity that are the same as those of the present Uranus, we have to assume that the atmosphere is more polluted than the envelope ( $x_{\text{btm}} = 0.5$  and  $Z_0 = 0.3$ , for example), which is hydrodynamically unstable, in principle. In the above scenario, icy materials are supplied to the geometrically thin atmosphere from the circumplanetary disk. The hydrodynamic stability of such a heavy, thin layer and the efficiency of ice material transport between the atmosphere and interior are to be examined by hydrodynamic simulations. Thus, to resolve the faint Uranus paradox within the scenario of accelerated cooling due to atmospheric pollution, the origin and stability of this distribution of the volatiles remains a crucial issue that is to be explained by future studies.

Note that the above hypothesis for the origin of the two different ice giants does not necessarily mean that there is a dichotomy between these two classes of ice giants in extrasolar systems. Planetary luminosity is a function of time, planetary mass, planetary radius, and composition. Even for planets with the same age, mass, and radius, the atmospheric composition will differ from planet to planet. This is partly because the outcome of a giant impact differs greatly, depending on the collisional angle and velocity. Thus, a continuum of luminosity, not a dichotomy, will be seen in extrasolar systems.

#### 4.2. Self-luminous Extrasolar Ice Giants

As mentioned in the Introduction, future observations are expected to directly detect the thermal emission of extrasolar ice giants. In this study we have found that ice giants, if their atmospheres are polluted with the volatiles, are much more luminous in early stages than predicted without atmospheric pollution. Thus, it would be interesting to quantify how large a difference the effect of atmospheric pollution yields in the planet-to-star contrast.

Here we estimate the contrast  $C$  as

$$C = \frac{\int_{\Delta\lambda} B_\lambda(T_{\text{eff}})d\lambda}{\int_{\Delta\lambda} B_\lambda(T_*)d\lambda}, \quad (31)$$

where  $B_\lambda$  is the Planck function for the wavelength  $\lambda$  and  $\Delta\lambda$  is the bandwidth, and  $T_{\text{eff}}$  and  $T_*$  are the effective temperatures of the planet and the host star, respectively. Figure 6 shows the estimated value of  $C$  for the ice giant at age 0.1 Gyr in the cases without pollution ( $x_{\text{btm}} = 0.023$ ; open circles) and with pollution ( $x_{\text{btm}} = 0.5$ ; open squares). The values of the other

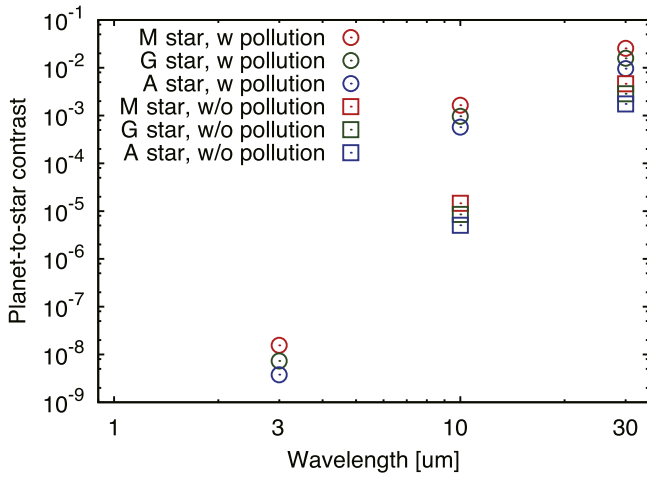


**Figure 6.** Predicted brightness contrast between the ice giant and the host star of age 0.1 Gyr (see Equation (31)). The assumed mass and equilibrium temperature of the ice giant are the same as those of Uranus (see Table 1). The open circles and squares represent the results with and without atmospheric pollution ( $x_{\text{pm}} = 0.023$  and  $0.5$ ), respectively. The symbols are colored according to stellar type, M-type ( $0.3 M_{\odot}$ ), G-type ( $1.0 M_{\odot}$ ), and A-type ( $1.8 M_{\odot}$ ) main-sequence stars. Note that low values of the contrast,  $C$ , at 1 and 3  $\mu\text{m}$  are not presented: for the non-polluted cases,  $C \sim 10^{-15}$  and  $10^{-42}$  at 1 and 3  $\mu\text{m}$ , respectively, and  $C \sim 10^{-23}$  at 1  $\mu\text{m}$  for the polluted case.

parameters are given in Table 1. We have considered different types of host stars, which include M-type ( $0.3 M_{\odot}$ ; red symbols), G-type ( $1.0 M_{\odot}$ ; green symbols), and A-type stars ( $1.8 M_{\odot}$ ; blue symbols). The evolution of the host star is calculated with the SSE package (Hurley et al. 2000). The wavelength  $\lambda$  is assumed to be 1, 3, 10, and 30  $\mu\text{m}$  with a bandwidth of  $\Delta\lambda = 0.2 \mu\text{m}$ .

Since planets are cooler than the host stars, the contrast becomes higher, in general, as the wavelength becomes longer. Thus, a longer wavelength is preferable for a direct detection. Moreover, since the polluted atmosphere of the ice giant is hotter ( $\sim 250$  K) than the non-polluted atmosphere ( $\sim 140$  K) in the early stages, the contrast for the former (open circles) is higher than that for the latter (open squares). Furthermore, the contrast difference between the polluted and non-polluted atmospheres decreases as the wavelength increases, as shown in Figure 6. This means that to distinguish between the two types of atmospheres, intermediate wavelengths are preferable. Indeed, in Figure 6, it is found that the difference is about two orders of magnitude at  $\lambda = 10 \mu\text{m}$ ;  $C \sim 10^{-5}$  for the non-polluted case, whereas it is  $C \sim 10^{-3}$  for the polluted case. It is interesting to note that the detection level for high-contrast imaging with MIRI on the *JWST* is  $\sim 10^{-4}$  for 1 arcsec (Beichman et al. 2010). While evaluating the actual detectability via direct imaging is beyond the scope of this study, the simple analysis done here is sufficient to indicate that a detailed investigation is quite important.

#### 4.3. Caveats

In this study we have made some simplifications. First, while we have assumed that the structure is completely adiabatic (or iso-entropic) in the convective regions of the atmosphere, in reality it is not exactly adiabatic, but super-adiabatic. In particular, if the compositional gradient is large enough to efficiently prevent convection from transporting entropy from

the deep interior, the temperature gradient is super-adiabatic, which was pointed out by Guillot (1995) in the case of the giant planets. Inefficient convections that delay planetary cooling include layered convection, in which mode small convective cells are separated by diffusive interfaces (Radko 2003; Rosenblum et al. 2011; Mirouh et al. 2012; Wood et al. 2013). The transport efficiency of the layered convection depends on the layer thickness. The impact of the layered convection on the thermal evolution was recently examined in the case of gas giants by Vazan et al. (2015), Kurokawa & Inutsuka (2015), and Nettelmann et al. (2015). They showed that the layered convection was hydrodynamically unstable against large-scale overturning convection, resulting in smoothing out the compositional inhomogeneity in the planetary interior. As mentioned in the Introduction, although theories predict that convection should be inhibited in the atmospheres of Uranus and Neptune (Guillot 1995; Leconte et al. 2016),  $\text{CH}_4$  clouds, which are formed by convection, are also observed there. Our assumption of pseudo-moist convection in the atmosphere is supported by the recent hydrodynamic study by Li & Ingersoll (2015), who showed that the atmospheric temperature gradient was determined approximately by the pseudo-moist adiabat. Their calculation is valid only for low mole fractions of ice constituents, however. Similar investigations need to be made to validate our assumption.

Second, we have ignored the effect of clouds on the thermal structure of the atmosphere. Since clouds absorb infrared radiation, the addition of clouds makes the atmosphere optically thicker, which causes the pressure at the photosphere to become lower. The temperature at the photosphere, which is in the moist convective region, is determined by the vapor pressure. Thus the presence of clouds lowers the photospheric temperature and in turn the emitted flux from the photosphere. Consequently, the cooling time is prolonged due to the effect of clouds. Clouds also affect the planetary radius because the presence of clouds increases the thickness of the atmosphere and delays the planetary cooling. The former effect is tiny because the height of the cloud level corresponds to only about 0.1% of the planetary radius. We have also confirmed that the latter effect is not great enough to reproduce the present radius of Uranus. If the present luminosity of Uranus is reproduced, the atmosphere contains 50 mol% of ice constituents (see Figure 5). However, as shown in Figure 4, the planetary radius varies at most 10% between  $10^8$  and  $10^{10}$  years. This means that the radius is at most  $3.8 R_{\oplus}$ , which is smaller than Uranus. The detailed treatment of clouds is beyond the scope of this study. However, since the effect would have a non-negligible impact on the thermal evolution of ice giants, this is an important issue to be addressed in future studies.

## 5. Conclusions

Here we have quantified the effect of latent heat for the condensation of  $\text{H}_2\text{O}$ ,  $\text{NH}_3$ , and  $\text{CH}_4$  in the atmosphere on the thermal evolution of ice giants for the first time. We found out that the latent heat keeps the atmosphere warm and the planetary thermal emission high. Integrating the thermal evolution of ice giants with this effect, we demonstrated that ice giants with atmospheres highly enriched in those condensable species are significantly bright in early evolution stages and thereby evolve on short timescales, which means that the aged ice giants are less bright than predicted by



previous theories. We also found that the evolution timescale is sensitive to the amount of condensable constituents in the atmosphere. Our finding of such a rapid thermal evolution sheds light on the long-standing issue that Uranus is much less bright than theoretically predicted and is different in brightness from Neptune in spite of the similarity in mass and radius. Our finding that young ice giants with enriched atmospheres are quite luminous is also important for detecting extrasolar ice giants by direct imaging.

We thank Y. Abe and K. Hamano for fruitful discussions about the atmospheric structure. We also thank Y. Sekine for constructive comments on the manuscript. We also thank the anonymous referee for the careful reading and constructive comments that helped us improve this paper greatly. This work is supported partly by JSPS Core-to-Core Program “International Network of Planetary Sciences” and Grant-in-Aid for JSPS Research Fellow (No. 26-11515; K.K.), Scientific Research (A) (No. 16H02160; K.K.), for Scientific Research on Innovative Areas (No. 23103005; M.I.), and Scientific Research (C) (No. 25400224; M.I.).

## References

- Abe, Y., & Matsui, T. 1988, *JAtS*, **45**, 3081
- Atreya, S. K. 1986, *Atmospheres and Ionospheres of the Outer Planets and Their Satellites* (Berlin: Springer)
- Batalha, N. M., Rowe, J. F., Bryson, S. T., et al. 2013, *ApJS*, **204**, 24
- Beichman, C. A., Krist, J., Trauger, J. T., et al. 2010, *PASP*, **122**, 162
- Fortney, J. J., Ikoma, M., Nettelmann, N., Guillot, T., & Marley, M. S. 2011, *ApJ*, **729**, 32
- Fortney, J. J., & Nettelmann, N. 2010, *SSRv*, **152**, 423
- Freedman, R. S., Marley, M. S., & Lodders, K. 2008, *ApJS*, **174**, 504
- Guillot, T. 1995, *Sci*, **269**, 1697
- Guillot, T. 2010, *A&A*, **520**, A27
- Hori, Y., & Ikoma, M. 2011, *MNRAS*, **416**, 1419
- Hubbard, W. B. 1977, *Icar*, **30**, 305
- Hubbard, W. B., & Macfarlane, J. J. 1980, *JGR*, **85**, 225
- Hurley, J. R., Pols, O. R., & Tout, C. A. 2000, *MNRAS*, **315**, 543
- Inaba, S., Wetherill, G. W., & Ikoma, M. 2003, *Icar*, **166**, 46
- Ingersoll, A. P. 1969, *JAtS*, **26**, 1191
- Kobayashi, H., Tanaka, H., & Krivov, A. V. 2011, *ApJ*, **738**, 35
- Kuntz, M. 1997, *JQSRT*, **57**, 819
- Kurokawa, H., & Inutsuka, S.-i. 2015, *ApJ*, **815**, 78
- Kuzuhara, M., Tamura, M., Kudo, T., et al. 2013, *ApJ*, **774**, 11
- Lambrechts, M., & Johansen, A. 2014, *A&A*, **572**, A107
- Leconte, J., Selsis, F., Hersant, F., & Guillot, T. 2016, arXiv:1610.05506
- Li, C., & Ingersoll, A. P. 2015, *NatGe*, **8**, 398
- Lindal, G. F., Lyons, J. R., Sweetnam, D. N., Eshleman, V. R., & Hinson, D. P. 1987, *JGR*, **92**, 14987
- Lodders, K., Palme, H., & Gail, H.-P. 2009, *LanB*, **4**, 44
- Lyon, S. P., & Johnson, J. D. 1992, Los Alamos National Laboratory, Los Alamos, NM, LA-UR-92-3407
- Marley, M. S., Fortney, J. J., Hubickyj, O., Bodenheimer, P., & Lissauer, J. J. 2007, *ApJ*, **655**, 541
- Marley, M. S., & McKay, C. P. 1999, *Icar*, **138**, 268
- Matsui, T., & Abe, Y. 1986, *Natur*, **322**, 526
- Mirouh, G. M., Garaud, P., Stellmach, S., Traxler, A. L., & Wood, T. S. 2012, *ApJ*, **750**, 61
- Morbidelli, A., Tsiganis, K., Batygin, K., Crida, A., & Gomes, R. 2012, *Icar*, **219**, 737
- Nakajima, S., Hayashi, Y.-Y., & Abe, Y. 1992, *JAtS*, **49**, 2256
- Nettelmann, N., Fortney, J. J., Moore, K., & Mankovich, C. 2015, *MNRAS*, **447**, 3422
- Nettelmann, N., Helled, R., Fortney, J. J., & Redmer, R. 2013, *P&SS*, **77**, 143
- Nettelmann, N., Wang, K., Fortney, J. J., et al. 2016, *Icar*, **275**, 107
- Orton, G. S., Fletcher, L. N., Moses, J. I., et al. 2014a, *Icar*, **243**, 494
- Orton, G. S., Moses, J. I., Fletcher, L. N., et al. 2014b, *Icar*, **243**, 471
- Pearl, J. C., Conrath, B. J., Hanel, R. A., & Pirraglia, J. A. 1990, *Icar*, **84**, 12
- Podolak, M., & Helled, R. 2012, *ApJL*, **759**, L32
- Radko, T. 2003, *JFM*, **497**, 365
- Rosenblum, E., Garaud, P., Traxler, A., & Stellmach, S. 2011, *ApJ*, **731**, 66
- Rothman, L. S., Gordon, I. E., Babikov, Y., et al. 2013, *JQSRT*, **130**, 4
- Rothman, L. S., Rinsland, C. P., Goldman, A., et al. 1998, *JQSRT*, **60**, 665
- Sánchez-Lavega, A., Pérez-Hoyos, S., & Hueso, R. 2004, *AmJPh*, **72**, 767
- Saumon, D., Chabrier, G., & van Horn, H. M. 1995, *ApJS*, **99**, 713
- Slattery, W. L. 1992, *Icar*, **99**, 167
- Spergel, D., Gehrels, N., Baltay, C., et al. 2015, arXiv:1503.03757
- Stevenson, D. J. 1982, *AREPS*, **10**, 257
- Valencia, D., Ikoma, M., Guillot, T., & Nettelmann, N. 2010, *A&A*, **516**, A20
- Valencia, D., Sasselov, D. D., & O’Connell, R. J. 2007, *ApJ*, **656**, 545
- Vazan, A., Helled, R., Kovetz, A., & Podolak, M. 2015, *ApJ*, **803**, 32
- Venturini, J., Alibert, Y., Benz, W., & Ikoma, M. 2015, *A&A*, **576**, A114
- Wood, T. S., Garaud, P., & Stellmach, S. 2013, *ApJ*, **768**, 157